Study on the non-linear deformation and failure characteristics of EPS concrete based on CT-scanned structure modelling and cloud computing

Xianhui Feng [a], Bin Gong [a,b,*], Chun'an Tang [a], Tao Zhao [b]

[a] State Key Laboratory of Coastal & Offshore Engineering, Dalian University of Technology, Dalian 116024, China
[b] Department of Civil and Environmental Engineering, Brunel University London, London UB8 3PH, United Kingdom

ARTICLE INFO

ABSTRACT

To understand the complex deformation features and failure mechanisms of expanded polystyrene (EPS) concrete and reveal the composite effect of expanded polystyrene beads and polypropylene fibers, a series of experiments were conducted on the poured EPS concrete specimens. Meanwhile, a cloud computing system for 3D realistic failure process analysis (RFPA3D) was established to model the fine failure process of a real concrete structure. The micromorphology of the EPS concrete specimens was obtained via CT scanning and further processed using digital image processing technology. The Otsu algorithm was applied to automatically recognize the segmentation thresholds of each partition image and a procedure for CT image processing was designed to automatically realize digital image segmentation and merging. Then, the numerical models reflecting the microstructures of the EPS concrete specimens were built using the processed digital images and a series of 3D numerical simulations were performed using cloud-computing-based RFPA3D. The results show that for concrete with low EPS volume fracture, the non-smooth convex-step-shaped failure morphology, which is a typical brittle fracture characteristic, appears. In contrast, ductile fracture occurs for concrete with a high EPS volume fracture. Simultaneously, the addition of polypropylene fibers of a certain length can effectively prevent the formation and expansion of new cracks in the cement matrix. In addition, the peak strength of concrete increases with an increase in homogeneity while the residual strength generally decreases with an increase in homogeneity. Moreover, a more heterogeneous material presented more acoustic emission precursors before macro fracture. All these achievements greatly improve our knowledge of the design, construction, and maintenance of EPS concrete in civil engineering.

1. Introduction

In recent decades, the digital image processing (DIP) technology has been developed as an electronic method for manipulating digital images, generating visual signals, storing them as an array of pixel points, and extracting image information from them. DIP technology has been applied to analyze the microphysical properties of concrete materials, especially aggregate particle size and shape, since the 1990s. Lightweight concrete (LWC) is a multi-purpose material for construction, providing several technical,

* Corresponding author at: State Key Laboratory of Coastal & Offshore Engineering, Dalian University of Technology, Dalian 116024, China.
E-mail addresses: gongbin@dlut.edu.cn, bin.gong@brunel.ac.uk (B. Gong).

economical, environment-enhancing, and environment-preserving advantages, and is destined to become a primary construction material in the new millennium [1]. When expanded polystyrene (EPS) beads are used to produce LWC, they are typically referred to as EPS concrete [2]. Babavalian et al. (2020) [3] examined the simultaneous effects of EPS beads and polypropylene (PP) fibers on the tensile splitting, uniaxial compressive, and confined behavior of concrete by conducting 160 tests on cylindrical specimens. Sun and Wang (2015) [4] studied the pull-out failure process of reinforced concrete (RC) specimens, using an image-based modeling approach by considering random *meso*-structures within a material. The results show that their simulation can describe mesoscopic evolution in the pull-out process and effectively match the macroscopic load versus slip curve. Skarżyński et al. [2] conducted 2D simulations for four-phase concrete at the aggregate level, using an isotropic damage continuum model enhanced by the characteristic length of the microstructure and discrete element model.

Direct meshing of the mesoscale geometric model of concrete can effectively preserve the shape of concrete aggregates [5]. However, traditional methods for studying pore structure have displayed obvious disadvantages and limitations. For example, some are only suitable for characterizing pore sizes at a small scale [6] and some are only applicable when the camera is firmly fixed and the observed region is pre-painted with random patterns [7]. Besides, like most low load-bearing lightweight aggregates, the introduction of EPS beads to the concrete mixture reduces its compressive/tensile strength, as confirmed by previous studies [8–13]. Hence, some researchers have tried to compensate for the weakening effect of EPS beads by reinforcing EPS concrete with fibers [14–20]. The computed tomography (CT) scanning technology has proven effective for capturing the microstructure characteristics of concrete materials [21,22]. The CT-scanned results can provide accurate material structure data, which can be addressed by DIP to generate a series of interrelated images for numerical model establishment. However, to appropriately reproduce the three-dimensional (3D) microstructure details of concrete, a large number of elements need to be generated; this requires a high-performance computing resource and often cannot be satisfied by personal computers (PCs) [23]. However, cloud computing provides an effective solution to meet this demand. Cloud computing is regarded as a promising next-generation technology that delivers computing services — including servers, storage, databases, software, etc. — over the internet to offer fast innovation and flexible resources. According to the U.S. National Institute of Standards and Technology (NIST), the main advantage of cloud computing is its immediate accessibility, providing convenient access to a shared computing resource pool [24].

On the one hand, cloud computing is powerful and developers should ensure that software deployment adapts to the cloud platform to maximize computing power. On the other hand, cloud services allow external users to flexibly rent the required scale of computing resources that satisfy their needs, avoid purchasing expensive hardware equipment, and make full use of cloud computing configuration flexibility, which will surpass the current limitations of hardware and software resources. In the field of civil engineering, several researchers [25–30] have noted the prospect of further research combined with cloud computing, considering that infrastructure software of the future will no longer run on bare metal but on virtual machines. Although attempts have been made to build a structural health monitoring system based on a cloud computing platform, the application of cloud computing in civil engineering is not extensive and mainly concentrates on theoretical aspects [25,30,31]. Therefore, achieving real structure modeling and fine failure process simulation of EPS concrete using high computational efficiency and convenient resource allocation of cloud computing has
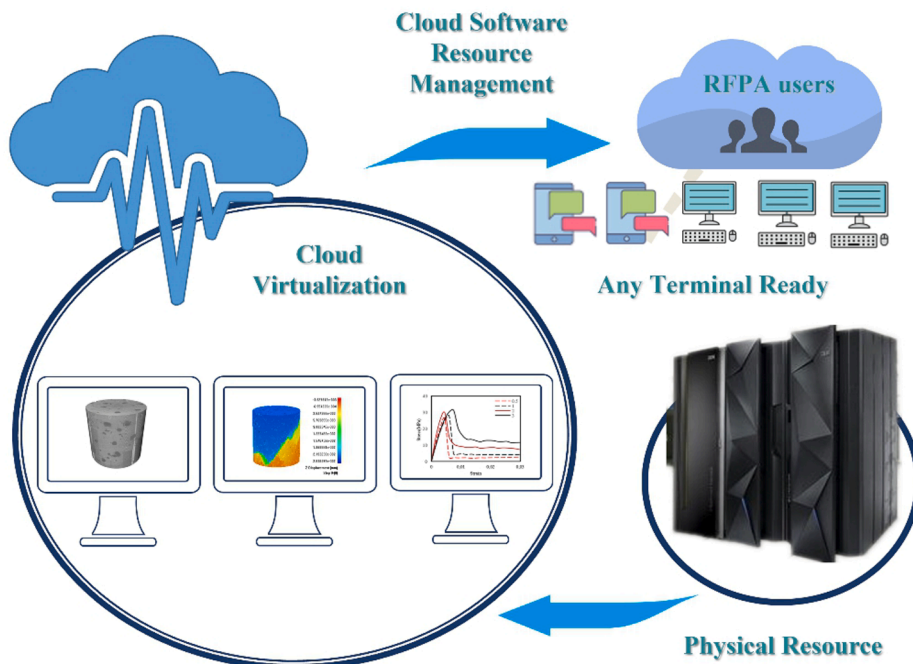

Fig. 1. High-performance cloud computing platform for RFPA3D simulation.

become a challenging and valuable topic in civil engineering.

Furthermore, most numerical simulations of concrete materials were conducted in two dimensions (2D). Concrete materials should be represented in 3D to properly reflect the mortar matrix and aggregate. Meanwhile, crack growth, similar to many fracture mechanical problems, is related to spatial scale and direction; i.e., it cannot be simplified into a 2D problem. In particular, for EPS concrete, the distribution of aggregates and EPS beads makes the failure evolution process much more complex. Thus, to reveal the failure mechanisms and strength characteristics of EPS concrete, the 3D realistic failure process analysis (RFPA3D) method [32,33] was applied to model progressive concrete fracture. RFPA3D has been developed based on continuum mechanics, statistical strength theory, and damage mechanics and, as a well-recognized numerical method, it has been extensively used to simulate crack initiation, propagation, and coalescence. The unique feature of the RFPA3D method is that there are no priori assumptions on where and how cracks/fractures will occur. In particular, cracking behavior can occur spontaneously and a variety of mechanisms will be exhibited when specific stress conditions are exceeded.

In this study, a series of poured specimens of EPS concrete were prepared to test the failure modes and peak strengths. The cloud computing system of RFPA3D was established to realize a fine simulation of the failure process of real concrete structures. The micromorphology of the EPS concrete specimens was obtained by CT scanning and the obtained images were analyzed using DIP. The Otsu algorithm was applied to automatically recognize the segmentation thresholds of each partition image and a procedure for CT image processing was designed to automatically realize digital image segmentation and merging. Then, numerical models reflecting the microstructures of the EPS concrete specimens were built using the processed digital images and a series of 3D numerical simulations were performed using RFPA3D. The reliability and effectiveness of the developed CT-based RFPA3D cloud computing method was verified through a comparison of the numerical and experimental results. The fracture mechanisms and diverse failure modes of EPS concrete were further studied.

2. RFPA3D cloud platform construction

2.1. Cloud computing environment configuration

The proposed cloud workstation and real-time online RFPA simulation system are shown in Fig. 1, from which we can see that any terminal device can access a supercomputer or high-performance server through the Internet. The RFPA program does not need to be installed on terminal devices. Instead, it can be accessed anytime and anywhere by opening a certain webpage and logging into a user account. In other words, low-cost terminal devices, such as laptops, tablets, and smartphones, can complete many complicated tasks that could only be achieved by large local computers in the past. The cloud server configuration contains up to 104-core Xeon platinum processors, 736 GB RAM, 10 PB storage space, and 40,960 CPU computing cores. Fast calculations of tens of millions of elements on the RFPA cloud platform can be initiated and monitored through personal terminal equipment.
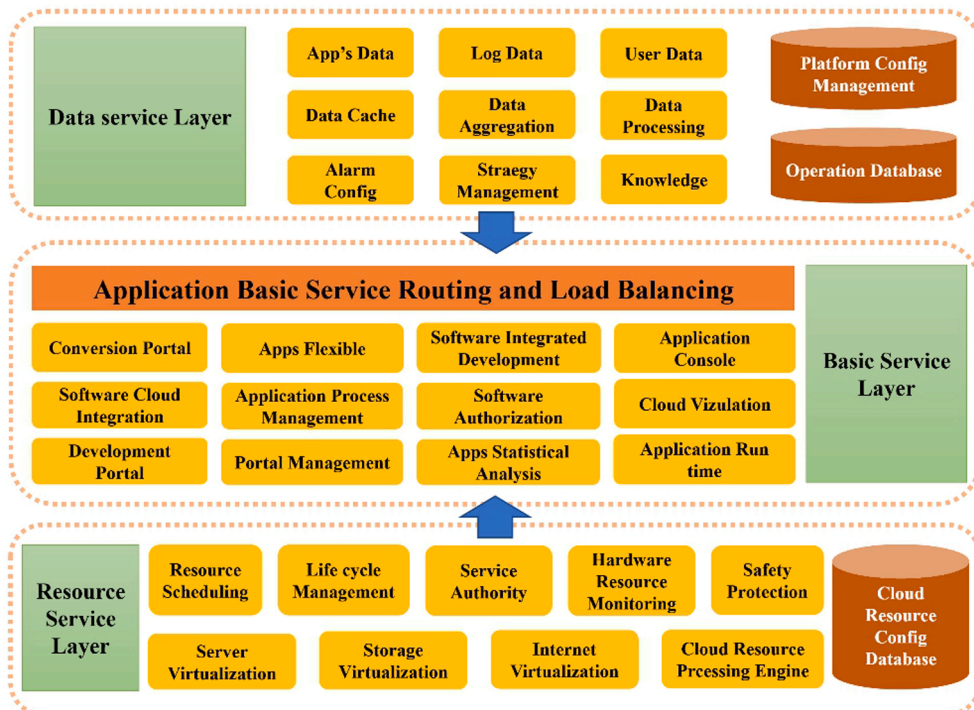

Fig. 2. RFPA cloud computing system.

2.2. Cloud computing performance testing

The main program of the RFPA3D system comprises four parts: the pre-processing module, finite element calculation module, failure analysis module, and post-processing module; among these, finite element calculation is the most time-consuming part of the analysis process. A detailed schematic of the developed RFPA cloud computing system is shown in Fig. 2.

With the help of cloud computing, the calculation scale and speed can be effectively increased. To test the performance of the cloud virtual machine, a series of cylindrical numerical models with the same diameter (50 mm) and height (75 mm) but different numbers of elements are built up. A cloud platform and personal computer were used to simulate the macro-fracturing of these models, induced by the initiation, development, and penetration of microcracks under uniaxial compression. The personal computer contains an Intel i7-10510 CPU, 16 GB RAM, and 1 TB storage space. A comparison of the single-step calculation time is shown in Fig. 3, from which it can be seen that the computational efficiency of cloud computing is much higher than a personal computer when the number of elements is more than one million. Note that as long as the configuration parameters are reasonable, the calculated results of the cloud server and personal computers should be the same, and the calculation accuracy remains unchanged.

3. Microstructure characterization and model establishment

3.1. CT image processing and material structure characterization

The purpose of DIP is to identify and characterize the shape and distribution of EPS particles and the concrete matrix using image threshold segmentation technology. In this section, the poured cylindrical concrete specimen is shown in Fig. 4. Meanwhile, the CT section of the cylindrical concrete specimen shown in Fig. 4 (d) is considered as an example. The image resolution is 100×100 pixels. EPS is of low density; therefore, it appears black in the CT-scanned image. The grayscale density of all the pixel points on the image is shown in Fig. 5. The principle of the grayscale threshold calculation is expressed in Eq. (1). In particular, if the gray value of a pixel point is lower than or equal to the threshold T_1, its gray value is set to be $1/(n + 1)$; if the gray value of the pixel point is greater than the threshold T_n, its gray value is set to 0.

$$f^{'}(x,y) = \begin{cases} 1/(n+1) & f(x,y) \leq T_1 \\ 2/(n+1) & T_1 < f(x,y) \leq T_2 \\ \vdots \\ n/(n+1) & T_{n-1} < f(x,y) \leq T_n \\ (n+1)/(n+1) & f(x,y) > T_n \end{cases} \tag{1}$$

where $f(x,y)$ is the initial gray value of the pixel point (x,y) and $f^{'}(x,y)$ is the gray value of the pixel point (x,y) after standardization. The gray histogram of the image and the generated grayscale grid are displayed in Figs. 5 and 6, respectively. In this study, the images were segmented according to gray thresholds to establish the numerical models.

3.2. Reconstruction of a 3D digital model of material structure

In this study, the pre-processing module of the RFPA3D program was used to build a 3D model reflecting the microstructural characteristics of EPS concrete. The 3D meshed numerical model was established by superimposing a series of processed images with a certain interval. For a continuous solid material, it is assumed that the slice image of the material specimen can represent the
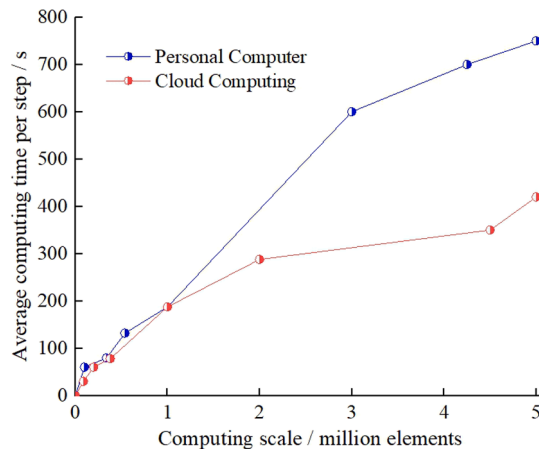

Fig. 3. Comparison of computational efficiency between PC and cloud computing.
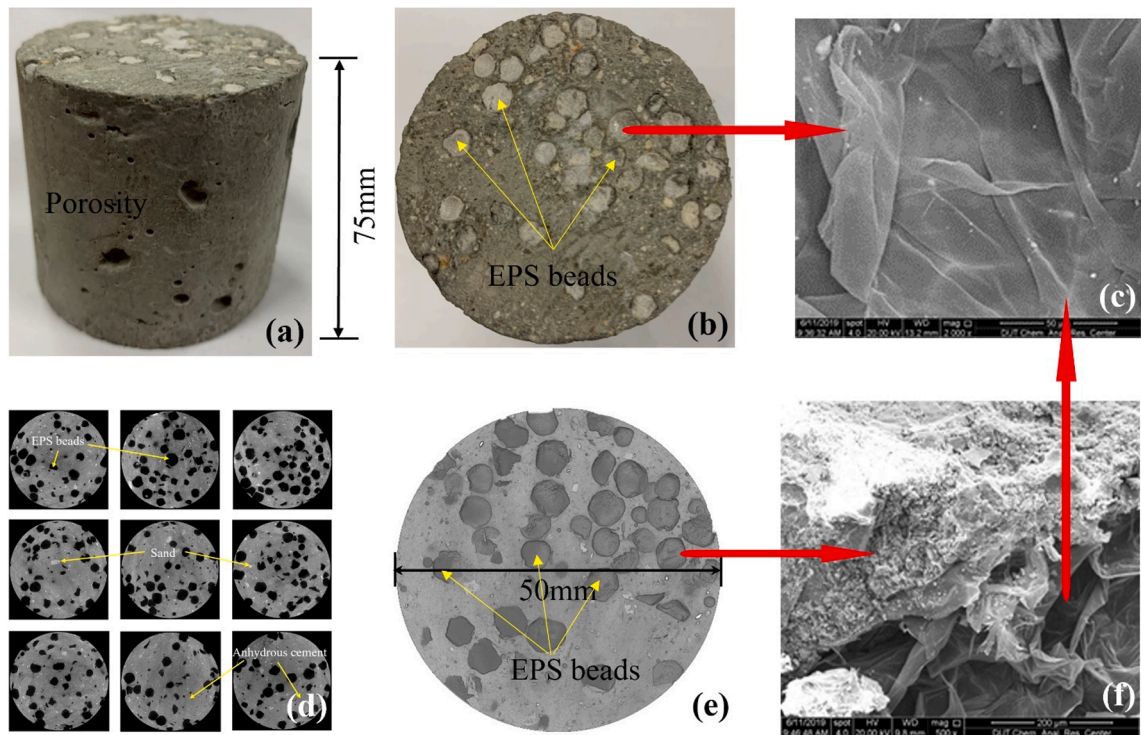
Fig. 4. The poured cylindrical concrete specimen: (a) appearance of the specimen, (b) visible EPS volume distribution, (c) surface micromorphology of EPS particles scanned by SEM, (d) different scanned sections by CT, (e) EPS volume distribution of the specimen processed by Avizo and (f) SEM observation of the interface transition zone between concrete and EPS particles.
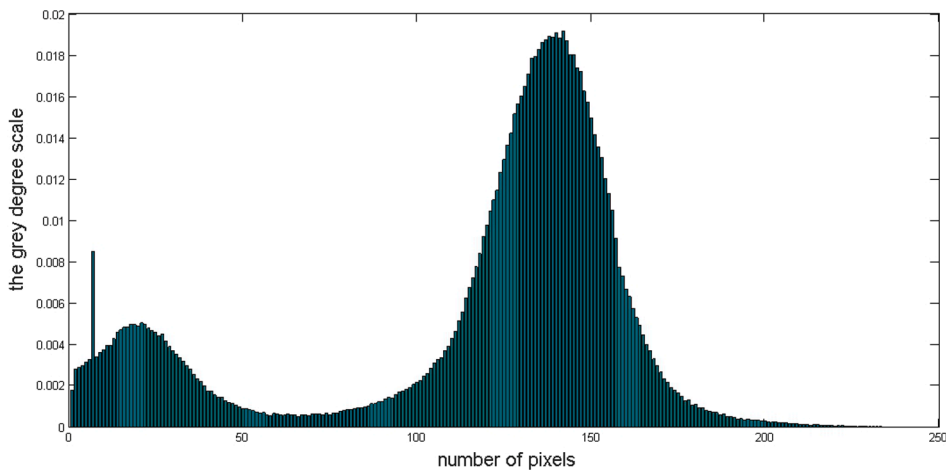

Fig. 5. Grayscale density of the image.

microstructure of the material with a small thickness t. To build a 3D numerical model, the image information needs to be converted into vectorized data. The digital image is composed of square pixel points, as shown in Fig. 6. In three-dimensional space, if the image is considered to have a default thickness t, each pixel point can be regarded as a finite element; i.e., the images can be compiled according to scanning order. Simultaneously, if the thickness t of each defined image is sufficiently small, the error between the 3D model and actual concrete specimen induced by meshing can be ignored. The vertex coordinates of each pixel point are transformed into the corresponding physical location in vector space (the thickness of each pixel point is t and the side length is l). According to the different standardized gray values of the pixel points, different concrete constitutions are identified, classified, and given related material parameters.

Fig. 6 shows the generation process of a 3D rectangular grid on the left-corner slice image of Fig. 4 (d). According to the above
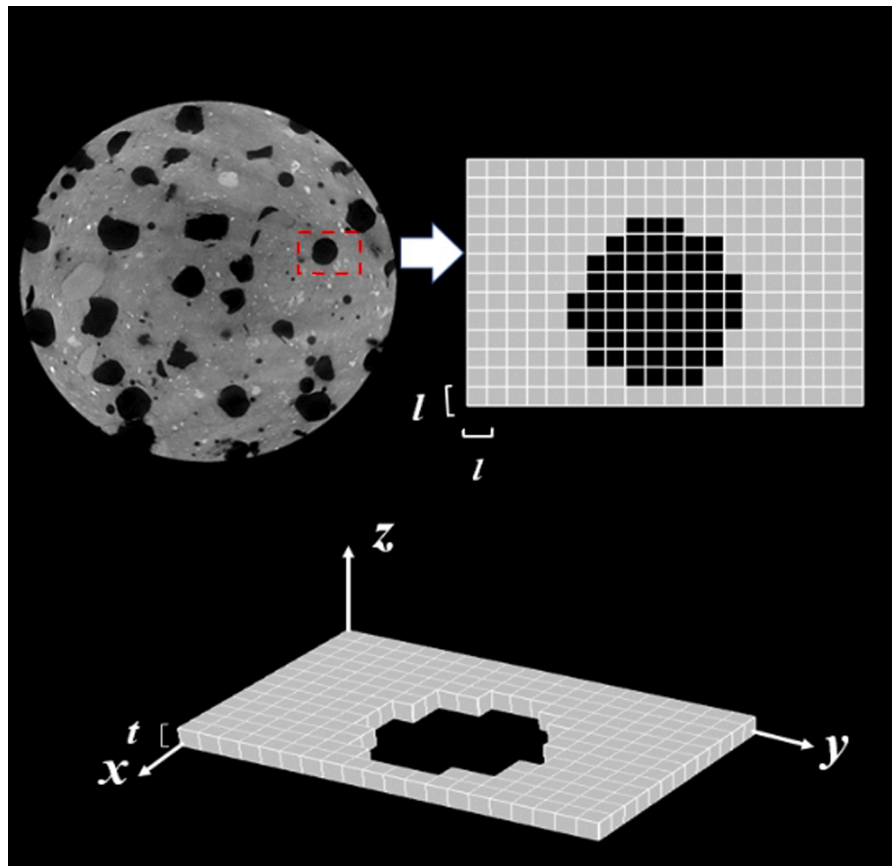
Fig. 6. The generated grayscale grid around one EPS bead.

transformation approach (from the representative image to the finite element grid), several 8-node hexahedral elements are generated using an image by the square pixel grid mapping method and the expanded thickness *t* is determined to be 1 mm. Fig. 7 shows the compilation process of the 3D mesh model, from which it can be seen that although the particles in the testing specimen were congested, with several small hexahedral elements and many edges and corners on the surface, the model reflected the real internal microstructure characteristics of the heterogeneous concrete materials to a large degree so that the detailed failure behavior of the actual material could be reproduced via numerical calculation.
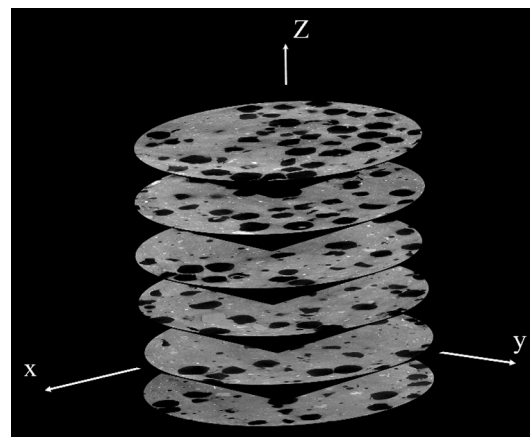

Fig. 7. The process of stacking CT images.

3.3. Heterogeneity of concrete

Heterogeneity plays a key role in governing the nonlinear deformation and failure behavior of concrete materials. Therefore, it should be considered appropriately. In this study, the statistical distribution function is introduced to describe the non-uniform distribution of the physical and mechanical parameters of concrete media. The element properties of the model, including the elastic modulus and strengths, are assumed to conform to the Weibull distribution [34] determined by Eq. (2), as follows:

$$f(u) = \frac{m}{u_0} \left(\frac{u}{u_0} \right)^{m-1} exp \left[-\left(\frac{u}{u_0} \right)^m \right] \tag{2}$$

where u is a given mechanical parameter (such as compressive strength, tensile strength, elastic modulus, or Poisson's ratio); u_0 is a scaling parameter related to the mean value of u; m is defined as the homogeneity index that determines the shape of the Weibull distribution function. As the homogeneity index m increases, the material becomes more homogeneous and vice versa [34].

Fig. 8 indicates the influence of the homogeneity index m on the shape of the probability density function of the Weibull distribution. Hence, m is also termed the Weibull shape parameter. Moreover, once the variables u_0 and m are determined, the physical and mechanical parameter values of model elements can be assigned using the Weibull parameter assignment method. Namely, the non-homogeneous parameter assignment of finite elements can be realized by generating a set of uniform random numbers, establishing the mapping from this set of numbers to a set of Weibull distribution random numbers (considering m), and determining the specific parameter values via the Weibull random numbers (considering u_0). Furthermore, to study the tensile failure and compression-shear failure characteristics of the material, the Mohr–Coulomb strength criterion with a tensile cutoff is adopted [32,35].

3.4. Mesoscopic element mechanical model for elastic damage

The progressive failure process of a concrete model subjected to loading can be described using damage mechanics. The elastic modulus of a damaged material is defined as follows:

$$E = (1 - \omega)E_0 \tag{3}$$

where ω is the damage variable. E and E_0 are the elastic moduli of the damaged and undamaged materials, respectively. The constitutive relationships of the elements under uniaxial compression and tension are shown in Fig. 9 [36,37].

The constitutive relationship of a mesoscopic element under uniaxial tension shown in the third quartile of Fig. 9 can be expressed as follows:

$$\omega = \begin{cases} 0 & \varepsilon > \varepsilon_{t0} \\ 1 - \dfrac{\lambda \varepsilon_{t0}}{\varepsilon} & \varepsilon_{tu} < \varepsilon \leq \varepsilon_{t0} \\ 1 & \varepsilon \leq \varepsilon_{tu} \end{cases} \tag{4}$$

where λ is the residual strength coefficient (which is defined as the ratio between the residual tensile strength f_{tr} and the initial tensile strength f_{t0}); ε_{t0} is the strain at the elastic tensile limit; ε_{t0} is the ultimate tensile strain of the element. The ultimate tensile strain is defined as $\varepsilon_{tu} = \eta \, \varepsilon_{t0}$, where η is the ultimate strain coefficient.

The equivalent principle strain ε is defined as follows:
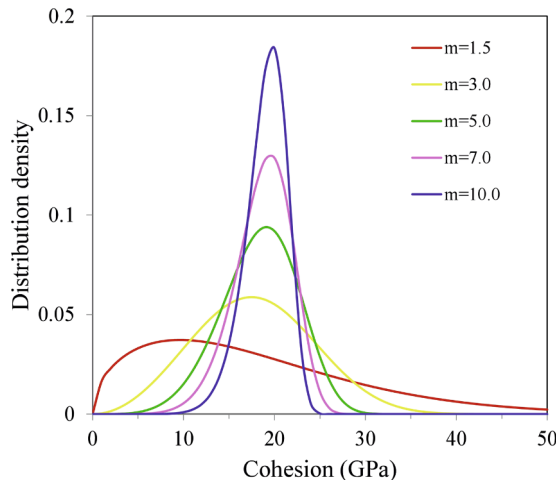

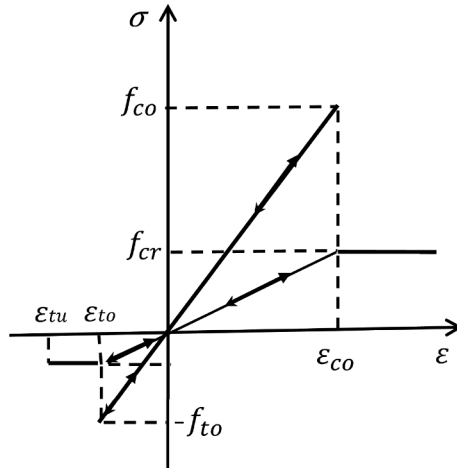**Fig. 8.** Distribution of element strength.

Fig. 9. Constitutive law of elements under uniaxial compression and tension.

$$\overline{\varepsilon} = -\sqrt{\langle-\varepsilon_1\rangle^2 + \langle-\varepsilon_2\rangle^2 + \langle-\varepsilon_3\rangle^2} \tag{5}$$

where ε_1, ε_2, and ε_3 are the maximum, intermediate, and minimum principal strains, respectively, and $<\,>$ is a function defined as:

$$\langle x \rangle = \begin{cases} x & x \geq 0 \\ 0 & x < 0 \end{cases} \tag{6}$$

The constitutive law of one element subjected to a multiaxial stress state can be easily obtained by substituting the strain ε in Eq. (4) with an equivalent principal strain $\overline{\varepsilon}$. The damage variable ω can be expressed as:

$$\omega = \begin{cases} 0 & \overline{\varepsilon} > \varepsilon_{t0} \\ 1 - \dfrac{\lambda \varepsilon_{t0}}{\overline{\varepsilon}} & \varepsilon_{tu} < \overline{\varepsilon} \leq \varepsilon_{t0} \\ 1 & \overline{\varepsilon} \leq \varepsilon_{tu} \end{cases} \tag{7}$$

To study the damage of elements when they are subjected to the compression-shear stress state, the Mohr–Coulomb criterion is chosen to determine the compression-shear failure point, expressed as follows:

$$F = \sigma_1 - \frac{1 + \sin\varphi}{1 - \sin\varphi}\sigma_3 \geq f_{c0} \tag{8}$$

where σ_1 and σ_3 are the major and minor principal stresses, respectively. f_{c0} is the uniaxial compressive strength and φ is the internal friction angle of the mesoscopic element. When the element is under uniaxial compression and damaged according to the Mohr–Coulomb criterion, the similar expression for the damage variable ω can be described as follows:

$$\omega = \begin{cases} 0 & \varepsilon < \varepsilon_{c0} \\ 1 - \dfrac{\lambda \varepsilon_{c0}}{\varepsilon} & \varepsilon \geq \varepsilon_{c0} \end{cases} \tag{9}$$

where λ is the residual strength coefficient. We assume that $f_{cr}/f_{c0} = f_{tr}/f_{t0} = \lambda$ is true when the element is under uniaxial compression or tension. When the Mohr–Coulomb criterion is met, the maximum compressive strain ε_{c0} at the failure point can be calculated using Eq. (10).

$$\varepsilon_{c0} = \frac{1}{E_0}\left[f_{c0} + \frac{1 + \sin\varphi}{1 - \sin\varphi}\sigma_3 - \mu(\sigma_1 + \sigma_2)\right] \tag{10}$$

In this study, it is assumed that the compression-shear damage evolution is related to the maximum compressive principal strain ε_1. Hence, we used the maximum compressive principal strain ε_1 of the mesoscopic element to substitute the uniaxial compressive strain ε in Eq. (9); hence, Eq. (9) can be extended to a multiaxial stress state for shear damage:

$$\omega = \begin{cases} 0 & \varepsilon_1 < \varepsilon_{c0} \\ 1 - \dfrac{\lambda \varepsilon_{c0}}{\varepsilon_1} & \varepsilon_1 \geq \varepsilon_{c0} \end{cases} \tag{11}$$

3.5. Numerical model setup

In this study, the size of the numerical models was 50 mm in diameter and 75 mm in height, as shown in Fig. 10. The total number of elements in the entire model exceeded 5 million. As the pore media, the concrete model is naturally composed of air elements [38]. To further discuss the influence of heterogeneity on the macro-mechanical response, a group of numerical tests were conducted. There were five specimens with different homogeneity indices m = 1.5, 2, 5, 7, and 10 loaded by uniaxial compression while the other parameters remained the same. Axial displacement loading was applied on the top surface along the z-axis, at a rate of 0.002 mm/s, and the bottom was fixed along the normal direction. The physical and mechanical parameters used for the modeling are listed in Table 1. Additionally, to reveal the effect of changing the height-diameter ratio on the failure pattern and peak strength of cylindrical specimens, a group of numerical models with different heights but the same diameter were established, as presented in Table 2.

4. Experimental and numerical result analysis

4.1. Physical experiment

4.1.1. EPS concrete specimen preparation

In this study, cylindrical concrete specimens were made with a size of 50 mm (diameter) × 75 mm (height). The mixture ratio of water, cement, sand, and aggregate was 1:2.02:2.73:5.54. Moreover, micro silicon powder was added to the concrete as a modified binder, considering that fine silica fume can increase the strength of EPS concrete (by 15 % at most) by improving the dispersion of EPS beads in the cement matrix and bonding between EPS beads and cement paste [39]. Meanwhile, PP fibers with a certain length and EPS beads with a diameter of 3 mm were used. The mix proportion of the fabricated concrete specimens is shown in Table 3, and the parameters of PP fiber and EPS bead are shown in Table 4. The poured specimens were cured in an incubator for 28 d. The concrete was made from ordinary Portland cement of Grade 42.5, produced in Dalian, China. Medium river sand (0.25–0.5 mm) was used as the fine aggregate, as shown in Fig. 4. As shown in Fig. 4 (b), the EPS volume distribution was random and discrete and Avizo software was used to calculate the porosity of the specimens in this study. The section of EPS concrete was further observed by scanning electron microscopy (SEM), as shown in Fig. 4 (c) and (f). From Fig. 4 (f), it can be observed that the interface of the modified EPS beads has good adhesion, under a magnification factor of 1000.

4.1.2. Analysis of stress–strain curve

Figs. 11 and 12 show the experimental results of the concrete specimens. Meanwhile, from Fig. 11 (c) and 12 (c), three typical stages can be observed in the stress–strain curve. First, in the elastic stage from the coordinate origin to the elastic limit, only a few small cracks were found on the surface of the specimen, the initial stress–strain curve was linearly elastic, and the axis strain increased with the increase in axis stress. Second, at the collapse stage from the elastic limit to the peak strength, more new cracks occurred at the existing micropores, cracks, interfaces between polystyrene particles and cement, and other defects because of the high-stress
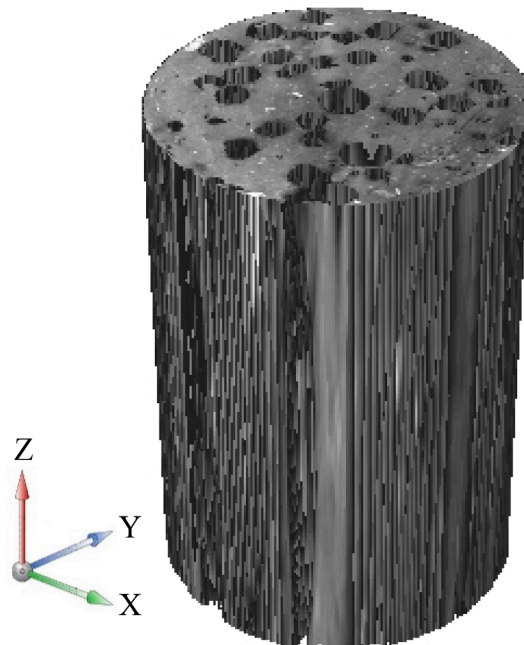

Fig. 10. Numerical model of EPS concrete.

Table 1

Physical and mechanical parameters used in the numerical simulations.

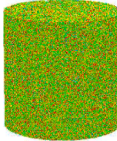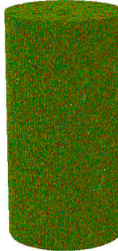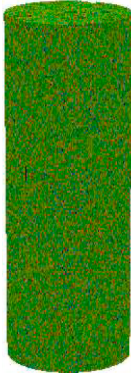| Parameters	Value
Elastic modulus (GPa)	30
Compressive strength (MPa)	200
Internal friction angle (°)	30
Ratio of compressive to tensile strength C/T	10
Poisson's ratio	0.25
Inhomogeneity index	1.5, 2, 5, 7, 10

Table 2

Geometry of the specimens.

Height/Diameter	0.5	1	2	3
Specimen name	size-1	size-2	size-3	size-4
Specimen for testing the effect of size				

Table 3

Mix proportion of fabricated concrete specimens.

Specimen No.	Water cement ratio (w/c)	Silicon powder (kg/m³)	EPS volume (%)	PP fiber length (mm)
M1	0.49	100	10	0
M2	0.49	100	20	0
M3	0.49	100	30	0
M4	0.49	100	40	0
M5	0.49	120	40	3
M6	0.49	120	40	6
M7	0.49	120	40	9
M8	0.49	120	40	12

Table 4

The physical and mechanical parameters of PP fiber and EPS bead.

Properties	PP fiber	EPS bead
Density (kg/m³)	900–920	25.7
Diameter (mm)	1	3
Length (mm)	3–12	–
Shape	Straight	Ball
Aspect ratio	545 [16]	–
Tensile strength (MPa)	400 [16]	–

concentration and low strength at these positions. Under continuous loading, newly formed cracks gradually developed. Polystyrene particles cannot prevent the continuous expansion of cracks. Instead, the interfaces between the polystyrene particles and cement provide potential paths for crack development. With an increasing number of cracks initiating and developing, macro-collapse occurs when the stress reaches its limit. Third, during the strain-softening stage from the peak strength to the residual strength, with continuous loading on the top of the specimen, the stress value rapidly drops to the residual strength after reaching the peak, indicating that the EPS concrete specimen loses its maximum bearing capacity. The degree of damage of the specimen becomes increasingly serious and the macroscopic fracture mode becomes increasingly obvious. Because the macroscopic strength is reduced by the
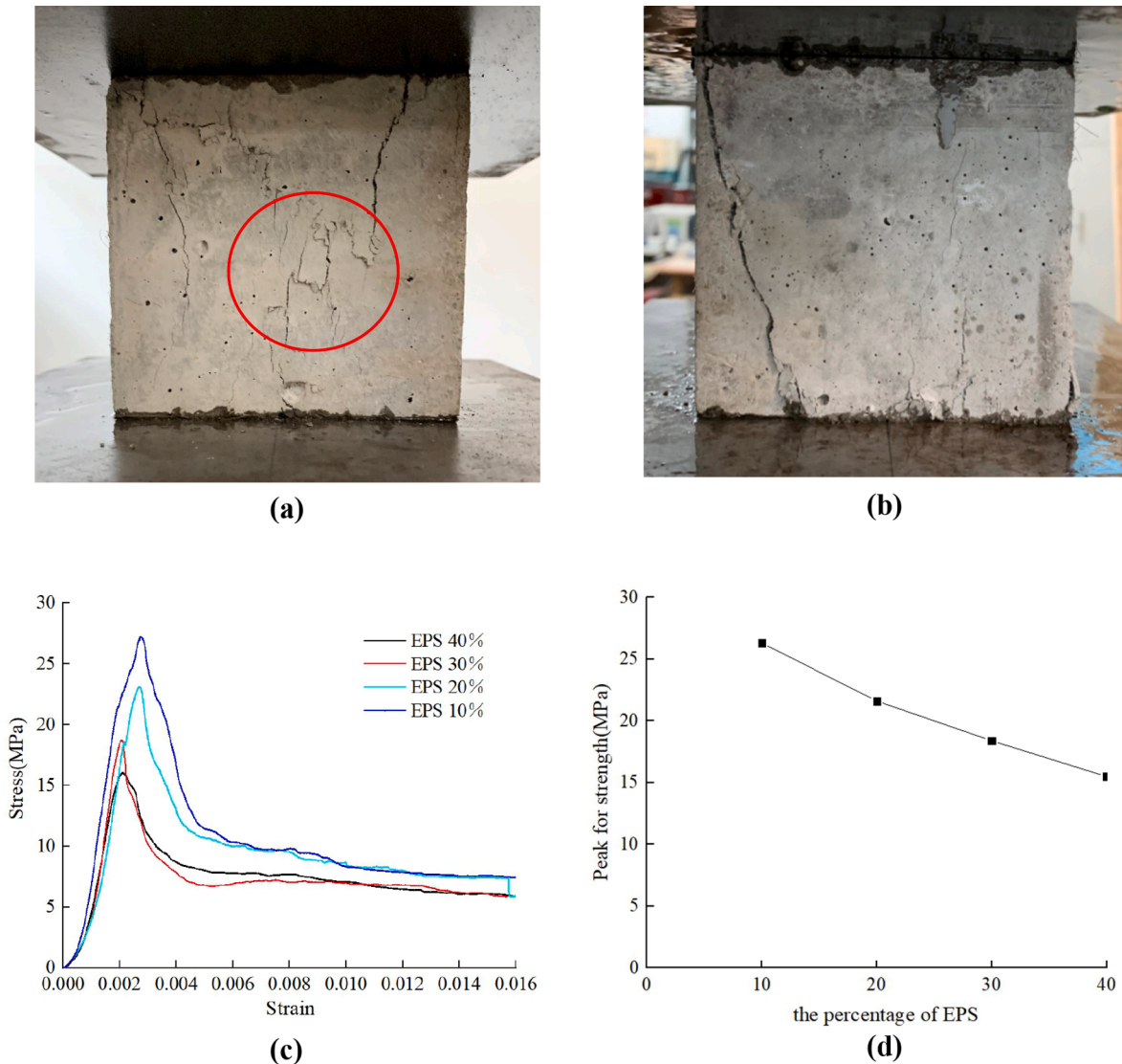
Fig. 11. Experimental results of the concrete specimens with different EPS volume fractions: (a) progressive failure process of Specimen I, (b) progressive failure process of Specimen II, (c) stress–strain curves and (d) peak strength curve.

embedded EPS beads, the EPS concrete cannot be fabricated into supporting members. After the peak strength is reached, the specimen bearing capacity generally drops sharply and then decreases at a slow rate. Regardless of the rapid dropping stage or slow decreasing stage, the axial strain continues to grow, indicating that the deformation modulus maintains a continuous decline.

4.1.3. Effect of EPS content on compressive strength

From the perspective of failure pattern formation, the failure process of concrete can be divided into three stages. In the first stage, several cracks, such as pores, microcracks, and bonding surfaces, were produced at the existing defects of the concrete. During the second stage, a large number of cracks developed stably and slowly due to the increase in external load. This stage is the stable propagation stage of the cracks. In the third stage, when these cracks connected to form macroscopic fractures, which dictated the specimen strength, the cracks entered the unstable growth stage. For the concrete containing a volume fraction of EPS beads, the expansion and combination of inner cracks were restricted owing to the existence of particles and the specimen exhibited ductile failure characteristics. For concrete containing a small volume fraction of EPS beads, the influence of particles on the combination of cracks is relatively small, indicating that brittle macroscopic fractures are more easily formed, eventually leading to the instability of the specimen.

Fig. 11 shows the experimental results of the concrete specimens with different EPS volume fractions under uniaxial compression, from which we can see that the fracture patterns, deformation laws, and strength characteristics of EPS concrete specimens are influenced by the volume fractions of the EPS beads. Clearly, for concrete with a relatively low EPS volume fracture, a convex-step-
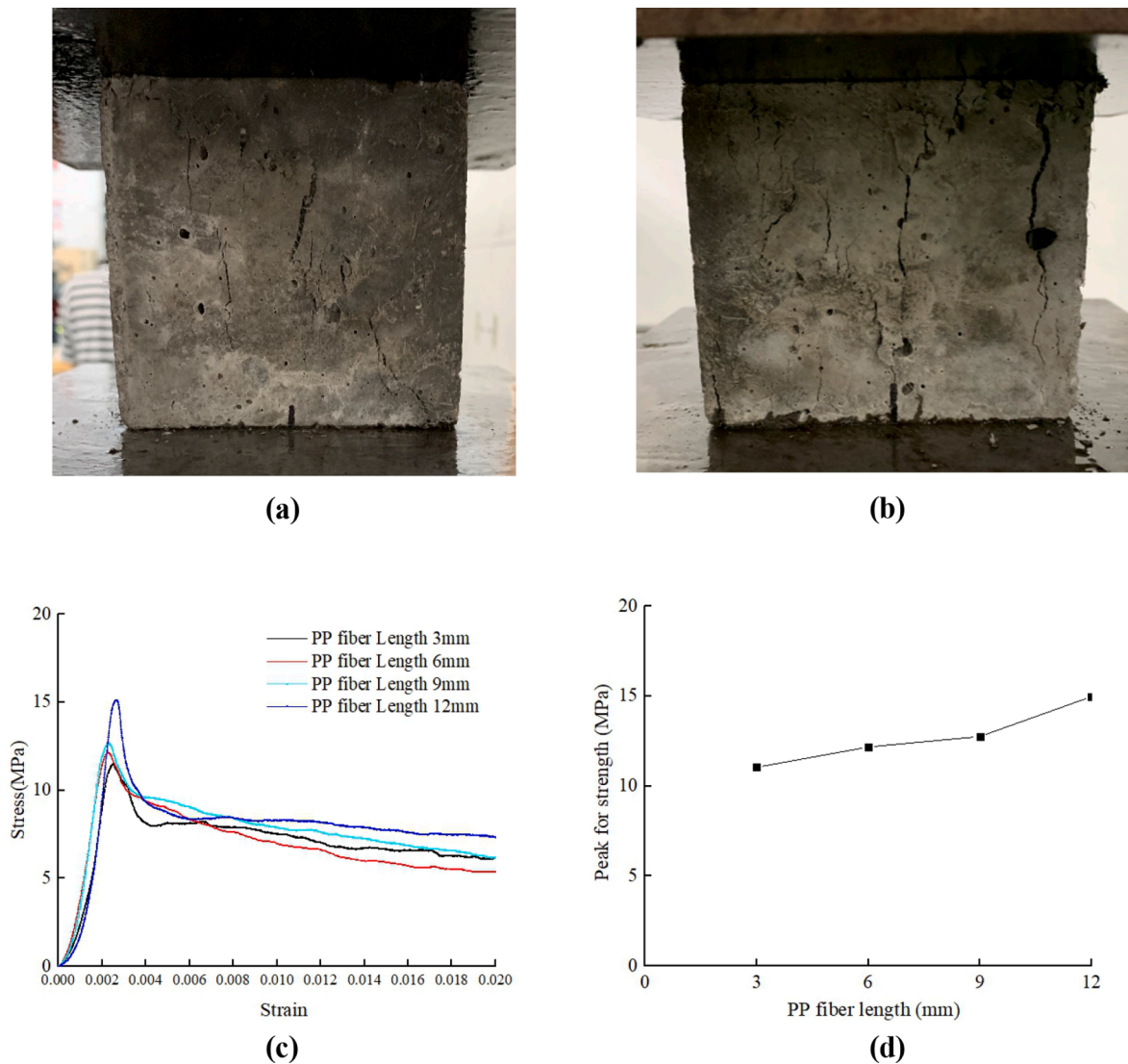
(a)

(b)

(c)

(d)

Fig. 12. Experimental results of the concrete specimens with different PP fiber lengths: (a) progressive failure process of Specimen I, (b) progressive failure process of Specimen II, (c) stress–strain curves and (d) peak strength curve.

shaped failure morphology appears. This non-smooth continuous crack propagation is a typical brittle fracture characteristic, as illustrated by [40] and reflects the internal mechanism of crack propagation. For concrete with a relatively high EPS volume fracture, the ductile fracture characteristics appear, as shown in Fig. 11 (b); this is mainly caused by a large number of microcracks distributed in the cement matrix around the particles and the specimen can continue to bear an external load until the final failure. Meanwhile, Fig. 11 (c) shows the stress–strain curves of concrete with different EPS volume fractures. Fig. 11 (d) indicates that the compressive strength of EPS concrete decreases almost linearly with the increase in EPS content, which is consistent with the results of other physical experiments [9,39]. This is because the increase in EPS content reduces the cement content per unit volume of the insulation mortar and therefore reduces the macroscopic strength.

4.1.4. Effect of polypropylene fiber length on compressive strength

Fig. 12 depicts the influence of different polypropylene fiber lengths on the 28 d compressive strength of foam concrete with the same EPS content. The EPS particle content used in this test was 40 % and the water-binder ratio was 0.5. The lengths of the polypropylene fibers used for each specimen were 3 mm, 6 mm, 9 mm, and 12 mm. As shown in Fig. 12 (d), the compressive strength of the concrete increases gradually with an increase in the polypropylene fiber length. When the fiber length is 6 mm, the 28 d compressive strength is 12.17 MPa; when the fiber length is 9 mm, the 28 d compressive strength is 12.75 MPa; and when the fiber length is 12 mm, the 28 d compressive strength is 14.977 MPa. However, the reinforcing effect of fibers with small lengths is not obvious. When EPS concrete is in the curing process, many microcracks are produced during the shrinkage hardening process. The addition of

polypropylene fibers of a certain length can effectively prevent the formation and expansion of new cracks in the cement matrix. Fig. 13 (b) shows the local enlarged drawing of polypropylene fiber-enhanced concrete, from which we can see that the polypropylene fibers penetrate through the EPS concrete from multiple directions, enhance the multidirectional tensile strength of the EPS concrete, and reduce the possibility of cracking. Polypropylene fibers of a certain length form a network structure in freshly mixed concrete, which effectively inhibits the segregation of EPS concrete.

4.2. Numerical simulation results of cloud computing

4.2.1. Crack evolution analysis

As shown in Fig. 14, under the uniaxial static compression load, dispersive microcracks first appear at the middle of the specimen. With the gradual increase in external load, these cracks begin to interpenetrate with each other at a 45° angle from the loading direction, extend to both ends of the specimen, and finally, break the specimen along the direction inclined near 45°. Notably, at the beginning of loading, high-stress concentrations occur at the existing pores, bonding surfaces, weaknesses, etc., where the initial cracks are generated. With the formation of initial cracks, the concentrated stresses are released and rebuilt at the tips of the cracks. This process is repeated and leads to continuous crack development. The phenomenon of continuous crack propagation and penetration can also be found in the experiments. Eventually, the specimen completely loses its bearing capacity. The fracture characteristics and instability modes agree with the physical tests.

Fig. 15 shows the damage and failure processes of EPS concrete specimen under uniaxial compression when the homogeneity $m = 7$. The green color represents that the elements have not undergone compression-shear or tensile failure while the red color indicates that the elements have failed, either in compression-shear mode or tensile mode. From the elastic modulus contours, it is clear that the weak elements in the concrete specimen begin to undergo damage first. Subsequently, an increasing number of elements are damaged and destroyed under further loading. The continuous process of stress buildup, stress release, and stress transfer leads to the formation of relatively small shear failure zones, as shown in Fig. 15 (b). With increasing loading, these failure zones gradually connect and form an obvious macroscopic shear fracture zone across the whole specimen, after the peak bearing strength of the specimen is reached.

4.2.2. Influence of heterogeneity on concrete failure

Fig. 16 shows the stress-induced progressive failure of the concrete specimens. Fig. 16 (a) and (c) clearly depict the various failure patterns and high-stress concentrated areas, respectively. Although 3D crack development cannot be observed directly, the spatial location and morphology of cracks can be captured by monitoring acoustic emission (AE) events. Fig. 16 (b) shows the spatial distribution of AE events, in which the center and radius of a ball represent the location and relative energy magnitude of a certain AE event. The red color represents the AE generated as the stress state of the element satisfies the tensile failure criterion and the blue color is therefore related to the compression-shear failure criterion. Moreover, according to the stress–strain curves of the concrete specimens with different heterogeneity shown in Fig. 17 (a), it can be found that when $m = 1.5$, many elements are damaged as early as at an axial strain of 0.0200041; when $m = 3$, many elements first fail at an axial strain of 0.0300164; when $m = 5$, the initial element failures occur at an axial strain of 0.0300164; when $m = 7$, some elements begin to undergo damage at an axial strain of 0.045016; when $m = 10$, some damaged elements occur for an axial strain of 0.0600329. They indicate that the linear elastic stage is longer for a more homogeneous concrete specimen. Fig. 17 shows that the peak strength of the specimen increases with the increase in homogeneity while the residual strength generally decreases with an increase in homogeneity. At the same time, with the increase in homogeneity, the higher the macroscopic strength, the steeper the descending portion of the post-peak curve. Moreover, the stress–strain curve shows the fluctuation feature at the residual stage because of the non-uniform gradual fracture process, which can also be found in the
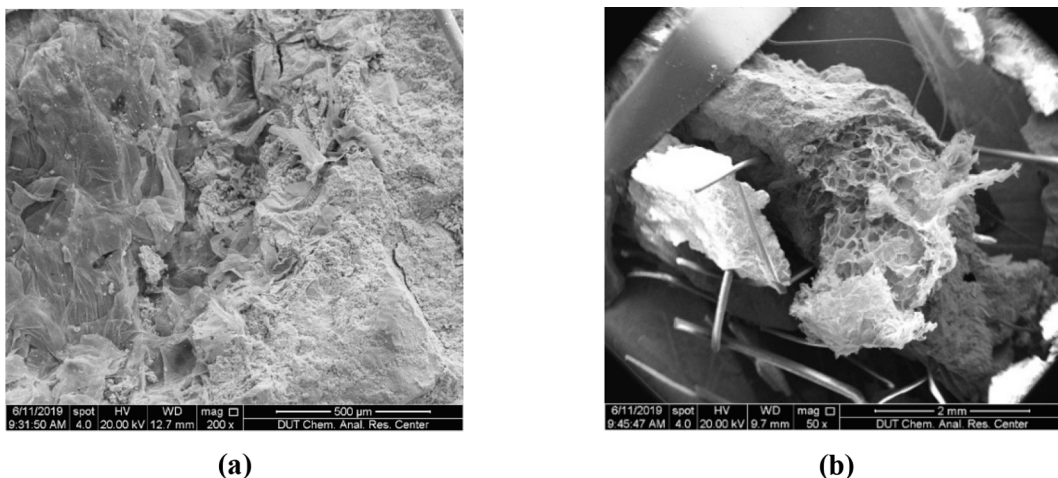

(a)   **(b)**

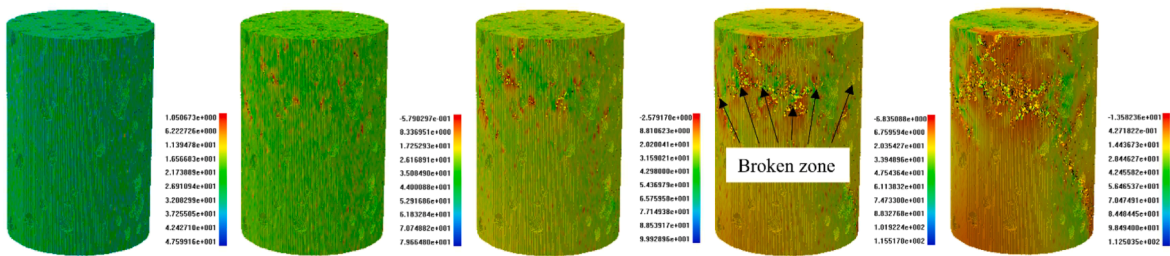**Fig. 13.** PP fibers observed by SEM: (a) magnification of 200 times and (b) magnification of 50 times.

Fig. 14. Maximum principal stress contour and macroscopic failure mode of EPS concrete.

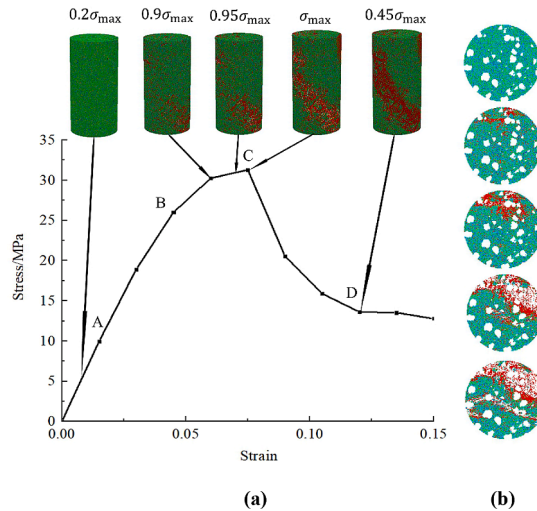**(a)**   **(b)**

Fig. 15. The damage and failure process of EPS concrete: (a) the stress–strain curve and failure process by elastic modulus contours and (b) the inner crack development at the middle section of the specimen.

previous tests.

4.2.3. Geometry effect on concrete failure

To investigate the influence of the slenderness ratio t, i.e., the ratio of height to diameter, on concrete failure, a series of cylindrical numerical models with the same diameter of the circle area but different heights were fabricated. As shown in Fig. 18, when the slenderness ratio is small, i.e., the model height is small, a single fracture cannot directly affect the resistance of the entire specimen, forming multiple main fracture features. With an increase in slenderness ratio t to 1.0, several macroscopic fractures also appear, except for the main fracture. When the slenderness ratio is $t = 2.0$, a macroscopic fracture comprising many small complex cracks appears. When the slenderness ratio is $t = 3.0$, a penetrating shear crack forms in the middle of the specimen. Furthermore, the slenderness ratio has a significant influence on peak strength and the process of concrete damage softening, as shown in Fig. 19. The bearing stress of a model with a small slenderness ratio suddenly decreases to a low level of residual strength after failure.

Fig. 20 shows the distribution of microcracks on different cross-sections of specimen $m = 7$ at critical failure. It can be seen that the cracks approximately distribute across the middle and lower parts of the specimen and there are many small branches on both sides of the main fracture. The macroscopic fracture plane penetrates the middle section and breaks the specimen, showing a typical compression-shear failure mode. The formation and penetration of the dominant failure surface is the main cause of the overall instability of the specimen.

### 4.2.4. Influence of heterogeneity on AE characteristics of concrete

The AE-axial strain curves of the concrete specimens with different heterogeneity are shown in Fig. 21, from which it can be seen that during the initial compaction stage, AE events mainly occur in the specimens with a low homogeneity index and the number of AE events gradually increases with an increase in loading. In addition, the smaller the homogeneity index, the greater the accumulative AE energy before macro-fracture, implying a greater degree of damage to the specimen. This phenomenon occurs because the dispersion degree of the material strength parameters is larger for a more heterogeneous material and more elements will be damaged under low stress. Meanwhile, the AE energy is released more quickly and forms a high peak during the critical failure stage. It is worth noting that a more heterogeneous material presents more AE precursors before the macro fracture, and for a more homogeneous material, the AE events are mainly caused by the final instability.
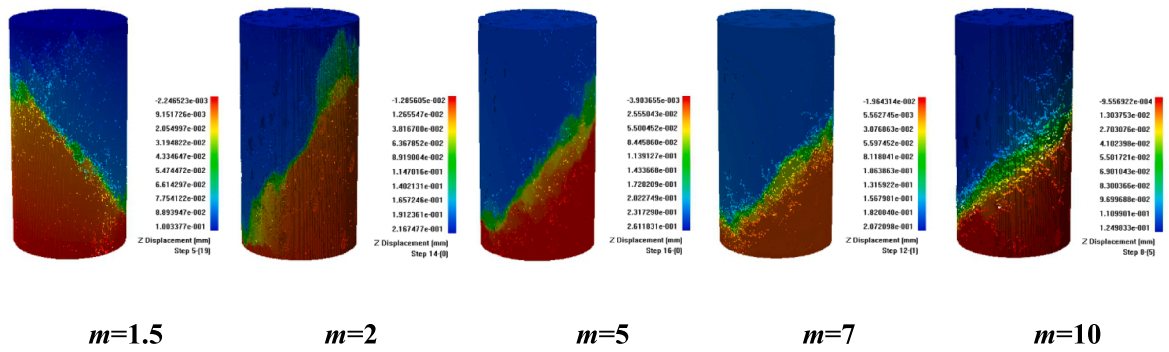
(a) Z-direction displacement contour
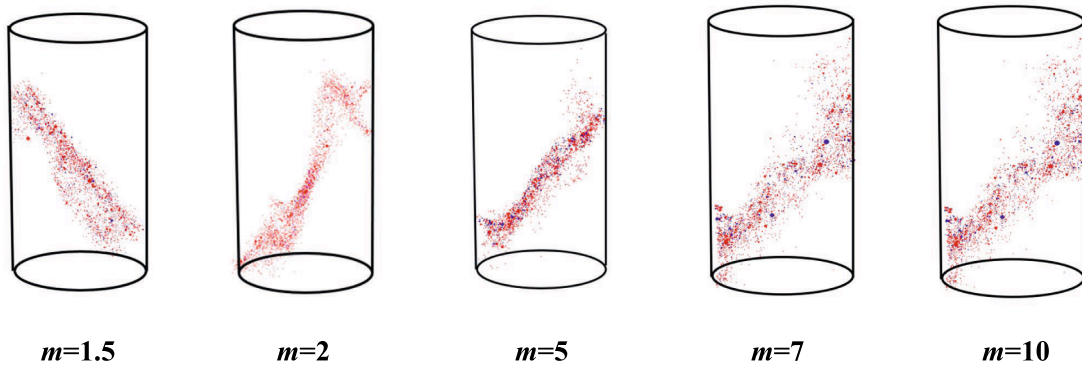
(b) Spatial distribution of acoustic emission events.
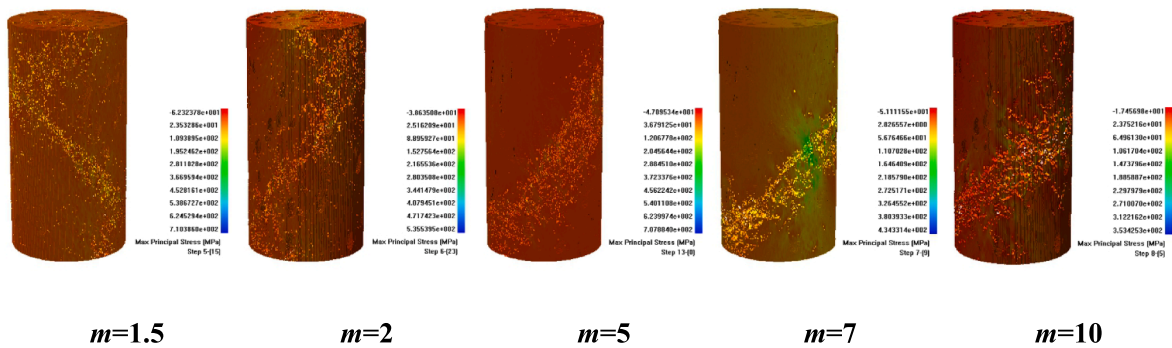
(c) Maximum principal stress contour

Fig. 16. The failure modes influenced by different homogeneity indexes *m*.

5. Conclusion

In this study, a series of poured EPS concrete specimens were prepared to study the failure modes and peak strengths and reveal the composite effect of EPS beads and PP fibers under uniaxial compression. Meanwhile, by combining cloud computing, CT scanning, digital image processing, and 3D realistic failure process analysis methods, a fine simulation of the failure process of real concrete structures is realized. The major findings and conclusions are summarized as follows.

Concrete specimens with different EPS volume fractions and PP fiber lengths were tested under uniaxial compression. First, the axial stress–strain curves can be divided into three main stages. In the elastic stage, only a few small cracks can be found on the surface of the specimen and the initial stress–strain curve is nearly linearly elastic; in the collapsed stage, many new cracks occur at the existing microcracks, pores, bonding surfaces between polystyrene particles and cement, and other defects because of the high-stress concentration and low strength at these positions; in the strain-softening stage, the concrete specimen loses its maximum bearing capacity
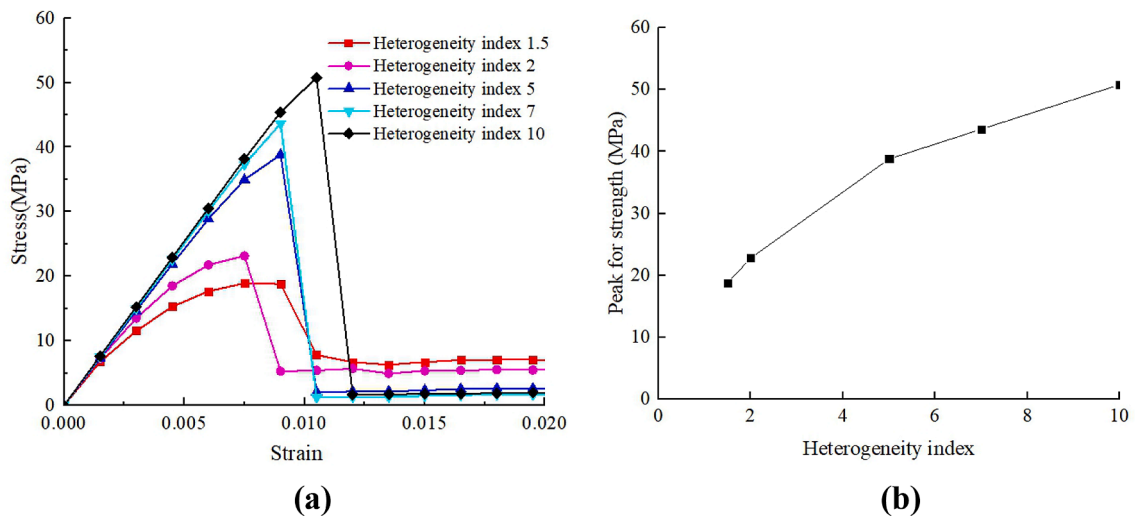
Fig. 17. (a) Stress–strain curves of different homogeneity indexes m and (b) relationship between peak strength and heterogeneity.
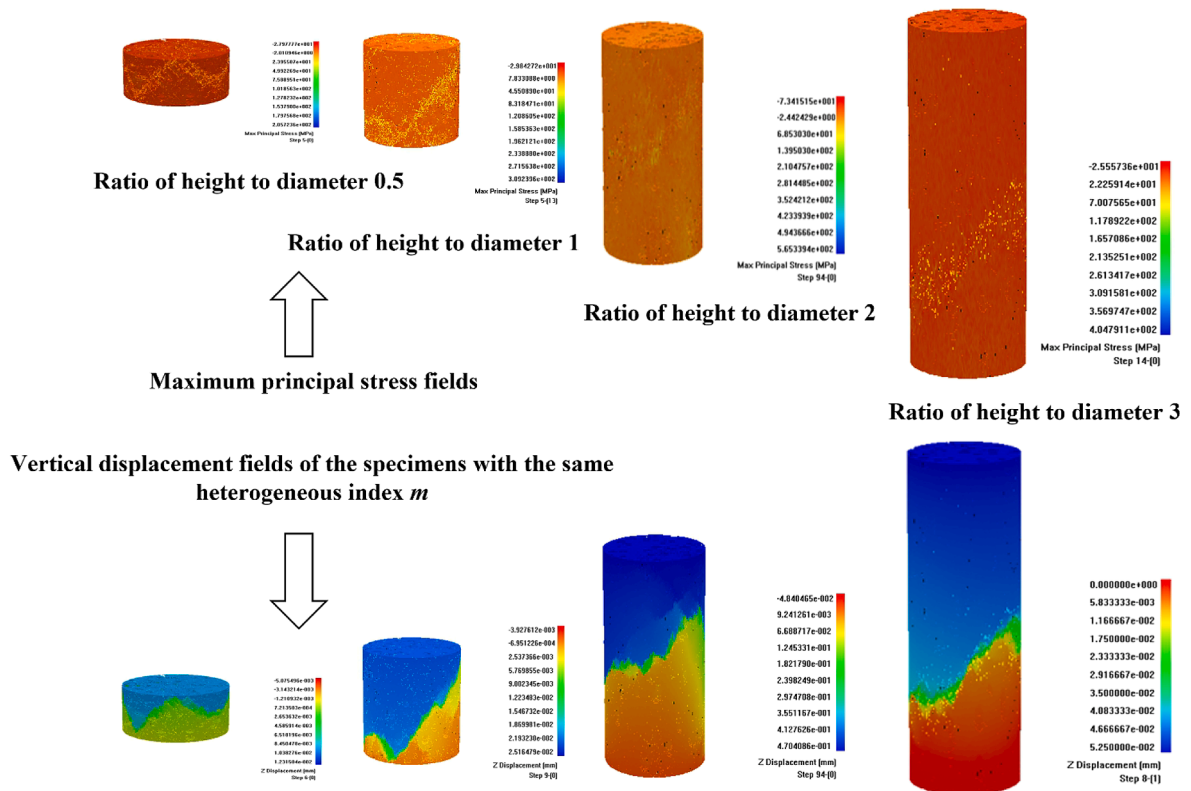

Fig. 18. Failure characteristics of four specimens with different slenderness ratios.

quickly, maintains the residual strength, and the axial strain continues to grow, indicating that the deformation modulus maintains a continuous decline. Second, for concrete with a low EPS volume fracture, the non-smooth convex-step-shaped failure morphology, as a typical brittle fracture characteristic, appears. In contrast, for concrete with a high EPS volume fracture, ductile fracture characteristics occur. Meanwhile, the compressive strength of EPS concrete decreases almost linearly with an increase in EPS content. Third, the experiments indicate that when PP-EPS concrete is in the curing process, many microcracks are produced during the shrinkage hardening process and the addition of polypropylene fibers of a certain length can effectively prevent the formation and expansion of new cracks in the cement matrix. Simultaneously, the compressive strength of EPS concrete gradually increases with an increase in
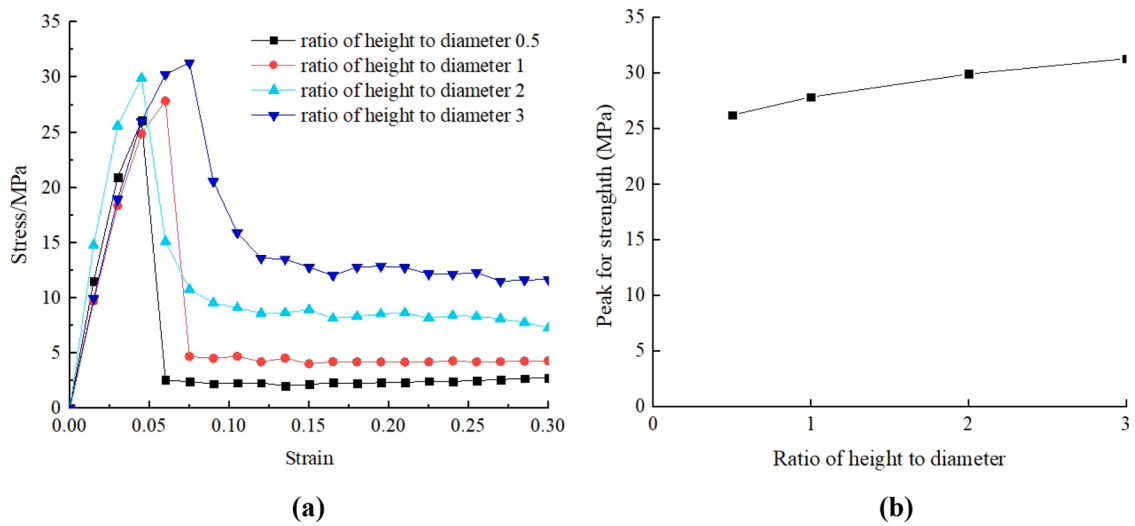
Fig. 19. (a) Stress-train curves of different slenderness ratios and (b) relationship between slenderness ratio and peak strength.
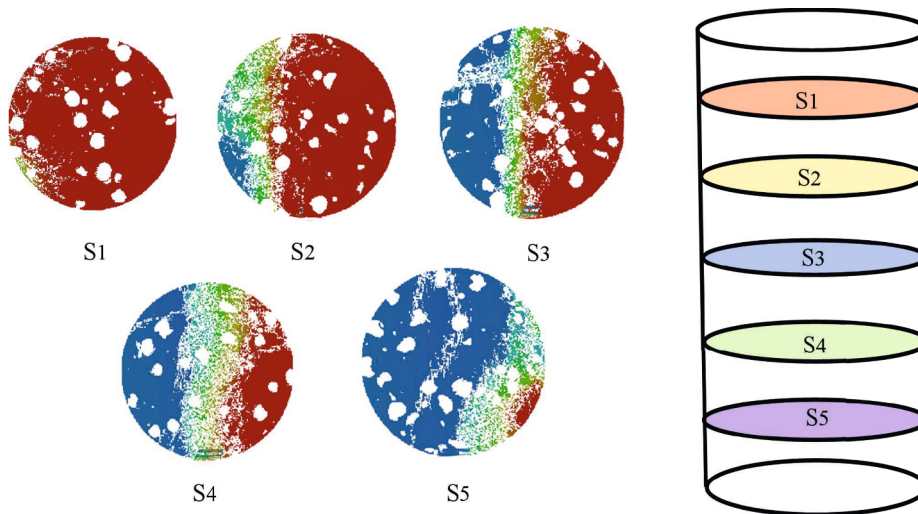

Fig. 20. Cracks on the section S1 – S5 at the peak failure state of the specimen with $m = 7$.

polypropylene fiber length.

Moreover, the cloud computing platform of RFPA3D was established to realize a fine simulation of the failure process of real concrete structures. The micromorphology of the EPS concrete specimen was obtained by CT scanning and the obtained images were analyzed by DIP. The Otsu algorithm was applied to automatically recognize the segmentation thresholds of each partition image and a procedure for CT image processing was designed to automatically realize digital image segmentation and merging. Then, the numerical models reflecting the microstructures of the EPS concrete specimen were built using the processed digital images and a series of 3D numerical simulations were therefore performed using RFPA3D. First, the linear elastic stage is longer for a more homogeneous concrete specimen and the peak strength of concrete increases with an increase in homogeneity while the residual strength generally decreases with an increase in homogeneity. Second, when the slenderness ratio is small, a single fracture cannot directly affect the resistance of the entire specimen and, when the slenderness ratio is large, a dominant shear crack controls the specimen stability. Third, a more heterogeneous material presents more AE precursors before macro-fracture. Additionally, cloud computing can effectively improve the computational efficiency of numerical simulations and overcome the limitations of hardware and software resources. All these achievements greatly improve our knowledge of the design, construction, and maintenance of EPS concrete in civil engineering.
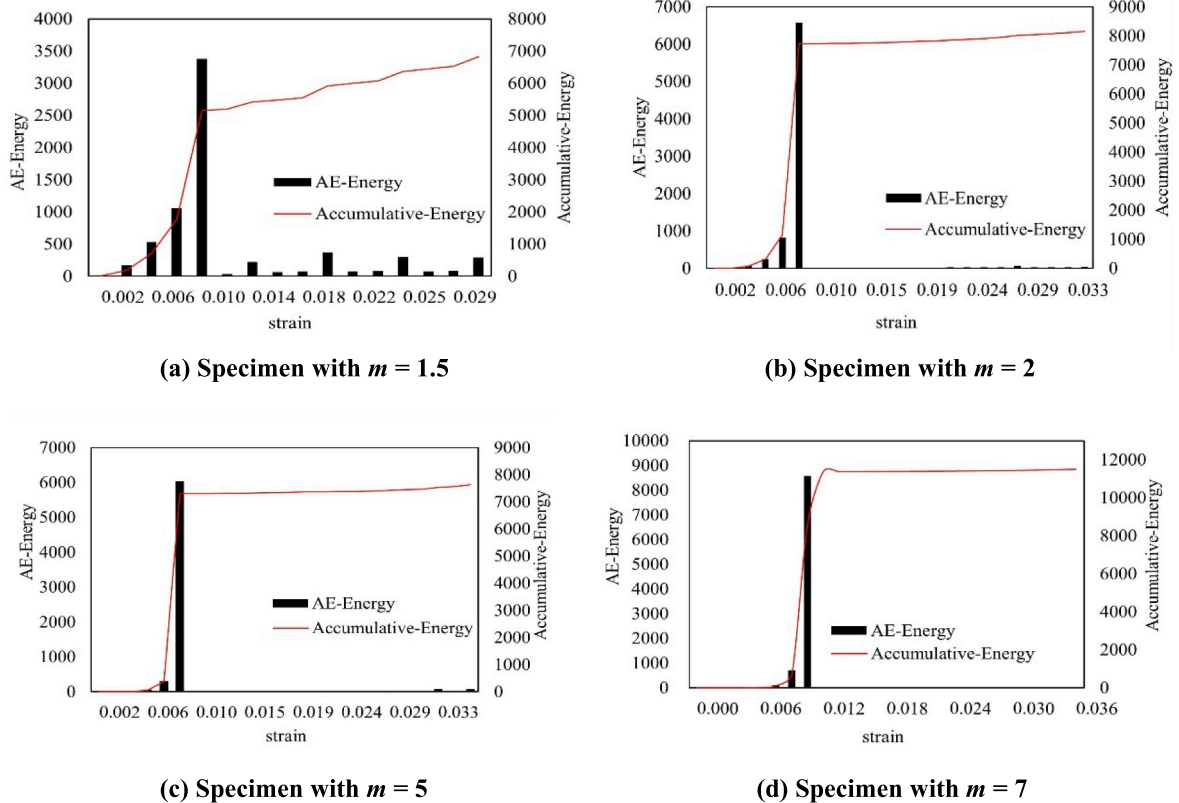
(a) Specimen with *m* = 1.5

(b) Specimen with *m* = 2

(c) Specimen with *m* = 5

(d) Specimen with *m* = 7

Fig. 21. AE energy characteristics influenced by different homogeneity indexes *m*.

CRediT authorship contribution statement

Xianhui Feng: Data curation, Investigation, Formal analysis, Writing – original draft, Validation. **Bin Gong:** Writing – review & editing, Supervision, Funding acquisition, Project administration, Methodology, Investigation, Conceptualization. **Chun'an Tang:** Resources, Software, Writing – review & editing. **Tao Zhao:** Writing – review & editing, Funding acquisition.

Declaration of Competing Interest

The authors declare that they have no known competing financial interests or personal relationships that could have appeared to influence the work reported in this paper.

Acknowledgements

References

[1] Haque MN, Al-Khaiat H, Kayali O. Strength and durability of lightweight concrete. Cem Concr Compos 2004;26(4):307–14.
[2] Skarżyński Ł, Nitka M, Tejchman J. Modelling of concrete fracture at aggregate level using FEM and DEM based on X-ray μCT images of internal structure. Engng Fract Mech 2015;147:13–35.
[3] Babavalian A, Ranjbaran AH, Shahbeyk S. Uniaxial and triaxial failure strength of fiber reinforced EPS concrete. Constr Build Mater 2020;247:118617. https://doi.org/10.1016/j.conbuildmat.2020.118617.
[4] Sun B, Wang X, Li Z. Meso-scale image-based modeling of reinforced concrete and adaptive multi-scale analyses on damage evolution in concrete structures. Comput Mater Sci 2015;110:39–53.
[5] Ouyang H, Chen X. 3D meso-scale modeling of concrete with a local background grid method. Constr Build Mater 2020;257:119382. https://doi.org/10.1016/j.conbuildmat.2020.119382.
[6] Zhou S, Sheng W, Wang Z, Yao Wu, Huang H, Wei Y, et al. Quick image analysis of concrete pore structure based on deep learning. Constr Build Mater 2019;208:144–57.

[7] Yang Y-S, Wu C-L, Hsu TTC, Yang H-C, Lu H-J, Chang C-C. Image analysis method for crack distribution and width estimation for reinforced concrete structures. Autom Constr 2018;91:120–32.
[8] Ramli Sulong NH, Mustapa SAS, Abdul Rashid MK. Application of expanded polystyrene (EPS) in buildings and constructions: a review. J Appl Polym Sci 2019.
[9] Mahdi HA, Jasim KA, Shaban AH. Manufacturing and improving the characteristics of the isolation of concrete composites by additive Styrofoam particulate. Energy Procedia 2019;157:158–63.
[10] Sadrmomtazi A, Sobhani J, Mirgozar MA, Najimi M. Properties of multi-strength grade EPS concrete containing silica fume and rice husk ash. Constr Build Mater 2012;35:211–9.
[11] Miled K, Sab K, Le Roy R. Particle size effect on EPS lightweight concrete compressive strength: experimental investigation and modelling. Mech Mater 2007;39 (3):222–40.
[12] Gomes MG, Flores-Colen I, Melo H, Soares A. Physical performance of industrial and EPS and cork experimental thermal insulation renders. Constr Build Mater 2019;198:786–95.
[13] Li C, Miao L, You Q, Hu S, Fang H. Effects of viscosity modifying admixture (VMA) on workability and compressive strength of structural EPS concrete. Constr Build Mater 2018;175:342–50.
[14] Banthia N, Majdzadeh F, Wu J, Bindiganavile V. Fiber synergy in Hybrid Fiber Reinforced Concrete (HyFRC) in flexure and direct shear. Cem Concr Compos 2014;48:91–7.
[15] Cao M, Zhang C, Lv H, Xu L. Characterization of mechanical behavior and mechanism of calcium carbonate whisker-reinforced cement mortar. Constr Build Mater 2014;66:89–97.
[16] Tabatabaeian M, Khaloo A, Joshaghani A, Hajibandeh E. Experimental investigation on effects of hybrid fibers on rheological, mechanical, and durability properties of high-strength SCC. Constr Build Mater 2017;147:497–509.
[17] Cao M, Xie C, Guan J. Fracture behavior of cement mortar reinforced by hybrid composite fiber consisting of CaCO3 whiskers and PVA-steel hybrid fibers. Compos A Appl Sci Manuf 2019;120:172–87.
[18] Pakravan HR, Latifi M, Jamshidi M. Hybrid short fiber reinforcement system in concrete: a review. Constr Build Mater 2017;142:280–94.
[19] Cao M, Xu L, Zhang C. Rheological and mechanical properties of hybrid fiber reinforced cement mortar. Constr Build Mater 2018;171:736–42.
[20] Chen B, Liu J, Chen L-Z. Experimental study of lightweight expanded polystyrene aggregate concrete containing silica fume and polypropylene fibers. J Shanghai Jiaotong Univ (Sci) 2010;15(2):129–37.
[21] Bouvard D, Chaix JM, Dendievel R, Fazekas A, Létang JM, Peix G, et al. Characterization and simulation of microstructure and properties of EPS lightweight concrete. Cem Concr Res 2007;37(12):1666–73.
[22] Maaroufi M, Abahri K, Hachem CE, Belarbi R. Characterization of EPS lightweight concrete microstructure by X-ray tomography with consideration of thermal variations. Constr Build Mater 2018;178:339–48.
[23] Yu Q, Liu H, Yang T, Liu H. 3D numerical study on fracture process of concrete with different ITZ properties using X-ray computerized tomography. Int J Solids Struct 2018;147:204–22.
[24] Mell P, Grance T. The NIST definition of cloud computing. Commun ACM 2011;53.
[25] Armbrust, Michael, Fox A, Armando, Griffith, Rean, et al. Above the clouds: a Berkeley view of cloud computing; 2009.
[26] Foster I, Zhao Y, Raicu I, Lu S. Cloud computing and grid computing 360-degree compared. Cloud Comput Grid Comput 360-Deg Compared 2009;5.
[27] Buyya R, Yeo CS, Venugopal S, Broberg J, Brandic I. Cloud computing and emerging IT platforms: Vision, hype, and reality for delivering computing as the 5th utility. Future Gen Comput Syst 2009;25(6):599–616.
[28] Sayadi AA, Tapia JV, Neitzert TR, Clifton GC. Effects of expanded polystyrene (EPS) particles on fire resistance, thermal conductivity and compressive strength of foamed concrete. Constr Build Mater 2016;112:716–24.
[29] Xie Y, Li J, Lu Z, Jiang J, Niu Y. Preparation and properties of ultra-lightweight EPS concrete based on pre-saturated bentonite. Constr Build Mater 2019;195: 505–14.
[30] Bai Z, Liu Y, Yang J, He S. Exploring the dynamic response and energy dissipation capacity of functionally graded EPS concrete. Constr Build Mater 2019;227: 116574. https://doi.org/10.1016/j.conbuildmat.2019.07.300.
[31] Vaquero LM, Rodero-Merino L, Caceres J, Lindner M. A break in the clouds: towards a cloud definition. Comput Commun Rev 2008;39(1):50–5.
[32] Tang C. Numerical simulation of progressive rock failure and associated seismicity. Int J Rock Mech Min Sci 1997;34(2):249–61.
[33] Tang CA, Kaiser PK. Numerical simulation of cumulative damage and seismic energy release during brittle rock failure—Part I: Fundamentals. Int J Rock Mech Min Sci 1998;35(2):113–21.
[34] Weibull W. A statistical distribution function of wide applicability. J Appl Mech 1951;18:293–7.
[35] Zhu WC, Tang CA. Micromechanical model for simulating the fracture process of rock. Rock Mech Rock Engng 2004;37(1):25–56.
[36] Zhu WC, Tang CA, Huang ZP, Liu JS. A numerical study of the effect of loading conditions on the dynamic failure of rock. Int J Rock Mech Min Sci 2004;41: 348–53.
[37] Liu HY, Kou SQ, Lindqvist P-A, Tang CA. Numerical studies on the failure process and associated microseismicity in rock under triaxial compression. Tectonophysics 2004;384(1-4):149–74.
[38] Liang ZZ, Xing H, Wang SY, Williams DJ, Tang CA. A three-dimensional numerical investigation of the fracture of rock specimens containing a pre-existing surface flaw. Comput Geotech 2012;45:19–33.
[39] Chen B, Liu J. Properties of lightweight expanded polystyrene concrete reinforced with steel fiber. Cem Concr Res 2004;34(7):1259–63.
[40] Lawn BR. Fracture of brittle solids. 2nd ed: Cambridge University Press; 1993.